

Dual reaction strategy for in-situ conductivity enhancement to enable high-performing aqueous zinc-based micro-batteries

Received: 4 February 2025

Accepted: 27 January 2026

Published online: 14 February 2026

Check for updates

Xinyi Xiu^{1,5}, Li Song^{2,5}, Meng Li¹, Xiangyang Li³, Zhonggui Quan², Xuting Jin¹✉, Liangti Qu⁴✉ & Zhen Zhou¹✉

Micro-batteries are promising candidates for powering various intelligent integrated applications. However, they typically rely on a single-cell reaction during charging and discharging cycles, limiting improvements in capacity and energy density. Here, we show an in situ conductivity enhancement-assisted double-cell reaction strategy to design high-performance Zn || Bi₂O₃@Ag₂O micro-batteries that integrate two sequential electrochemical reactions within a single microdevice. Unlike simply combining Zn || Ag₂O and Zn || Bi₂O₃ micro-batteries, this strategy leverages the in situ conductivity enhancement effect from the Ag₂O conversion reaction in the first step to significantly boost the discharge capacity (an almost order-of-magnitude improvement compared to Zn || Bi₂O₃ micro-batteries alone) of the second conversion reaction, resulting in a total capacity 2.1 times the combined discharge capacities of the two individual micro-batteries. Consequently, the constructed microdevice achieves a high energy density of about 19000 μWh cm⁻² and the microdevice also exhibits a micro-supercapacitor-level or higher power density (above 23000 μW cm⁻²). This work challenges conventional micro-battery configurations and offers a strategy for constructing high-performance micro-power sources for intelligent integrated electronics.

Miniaturized energy storage devices, such as micro-batteries (MBs) and micro-supercapacitors (MSCs), have garnered growing research interest owing to their potential applications in intelligent microelectronics, including micro-robotics, smart medical implants, intelligent electronic skins, deep-brain analysis, human activity monitoring, and wireless sensors^{1–5}. Due to their high power densities, excellent charge/discharge rates, and long cycle lifetimes, MSCs are expected to play a

pivotal role in these advanced fields. However, their areal energy density typically remains below 100 μWh cm⁻²^{6–8}, with some devices even falling below 10 μWh cm⁻²^{9,10}, significantly limiting their applications. To address these limitations, researchers are focused on developing MBs that offer higher energy density and more stable voltage output, thereby providing a reliable long-term energy supply for microelectronic devices.

¹Interdisciplinary Research Center for Sustainable Energy Science and Engineering (IRC4SE2), School of Chemical Engineering, Zhengzhou University, Zhengzhou, PR China. ²Henan Institute of Advanced Technology, Zhengzhou University, Zhengzhou, PR China. ³Key Laboratory of Cluster Science, Ministry of Education of China, Key Laboratory of Photoelectronic/Electrophotonic Conversion Materials, School of Chemistry and Chemical Engineering, Beijing Institute of Technology, Beijing, PR China. ⁴Key Lab of Organic Optoelectronics and Molecular Engineering of Ministry of Education, Department of Chemistry, Tsinghua University, Beijing, PR China. ⁵These authors contributed equally: Xinyi Xiu, Li Song. ✉e-mail: xutingjin@zzu.edu.cn; lqu@mail.tsinghua.edu.cn; zhengzhou@zzu.edu.cn

Subsequently, various advanced fabrication techniques such as screen printing, imprint lithography, and holographic lithography with conventional photolithography, have been employed to construct a series of organic lithium ion MBs composed of lithium titanate||lithium iron phosphate, lithium||V₂O₅ and nickel-tin||lithium manganate^{11–14}. However, the areal capacity and energy density of these organic lithium ion MBs remain below 200 $\mu\text{Ah cm}^{-2}$ and 360 $\mu\text{Wh cm}^{-2}$, respectively^{11–14}. In addition, organic dual-ion MBs, using graphite as both the positive and negative electrode with lithium hexafluorophosphate electrolytes, achieve a high energy density of 873.3 $\mu\text{Wh cm}^{-2}$ due to their high working voltage (-5 V)¹⁵. Moreover, organic sodium ion MBs have also been assembled using mask-assisted filtration and 3D printing techniques^{16,17}. Notably, 3D printing enables thick microelectrodes, allowing the sodium ion MBs to deliver high areal capacity of 4500 $\mu\text{Ah cm}^{-2}$ and high energy density 7330 $\mu\text{Wh cm}^{-2}$ ^{16,17}. Despite these advancements in electrochemical performance, the organic electrolytes used in these MBs present significant challenges due to their toxicity, volatility, and flammability, raising serious safety concerns and restricting their broader application.

Given the advantages of low cost, high theoretical capacity, and ease of operation in ambient conditions, researchers have increasingly turned to developing more environmentally-friendly and safer aqueous zinc-based MBs^{3,18,19}. To enhance the energy density of these MBs, a series of advanced positive electrode materials, including MnO₂^{3,20–24}, vanadium-based materials^{24–26}, polyaniline²⁴, NH₄CuHCF²⁷, LiMn₂O₄²⁸, LiFePO₄²⁸, Ni/Co materials^{29,30} have been explored. Unfortunately, due to the lack of a reasonable design, such as inadequate load improvement, suboptimal fabrication processes, insufficient exploration of new battery reactions, and inefficient utilization of the limited microelectrode footprint, the energy density achieved by these MBs remain below 1100 $\mu\text{Wh cm}^{-2}$ ^{3,20–30}. In terms of areal capacity, Wang et al. optimized ink formulations and printing parameters to effectively increase the loading of polyvinylpyrrolidone-induced ammonium vanadate nanobelt positive electrodes for Zn ions MBs using 3D printing technology, achieving high areal capacity of 4020 $\mu\text{Ah cm}^{-2}$ ³¹. Furthermore, in situ electrochemical deposition and dual-plating approaches have been proposed for the direct fabrication of Zn||I₂ and Zn||Br₂ MBs^{4,32}, attaining high areal capacity of 2220 $\mu\text{Ah cm}^{-2}$ and energy density of 3654 $\mu\text{Wh cm}^{-2}$. While these advances have significantly contributed to the progress of zinc-based MBs, a substantial performance gap persists when compared to the superior organic sodium-ion MBs. Moreover, for both the reported aqueous zinc-based MBs and organic lithium/sodium-ion MBs, the maximum reported areal capacity and energy density are still below 5000 $\mu\text{Ah cm}^{-2}$ and 7500 $\mu\text{Wh cm}^{-2}$, respectively (Fig. 1a)^{3–5,11–32}. Therefore, it remains highly challenging to develop a simple yet effective strategy to achieve high areal capacity above 15,000 $\mu\text{Ah cm}^{-2}$ and energy density of 15,000 $\mu\text{Wh cm}^{-2}$ for aqueous zinc-based MBs (Fig. 1a).

In most aqueous zinc-based MBs and organic lithium/sodium-ion MBs, a single charge-discharge cycle typically corresponds to the reversible redox reaction of one battery, limiting the potential for significant breakthroughs in capacity and energy output per unit area (Fig. 1a). To meet higher energy demands, these MBs must be connected in series or parallel, which increases the overall footprint of microdevices, reduces space efficiency, and leads to excessive material waste. The strategy of integrating double-cell electrochemical reactions within a single battery offers a promising solution to this challenge. However, the successful implementation of this approach requires the fulfillment of several critical conditions. First, the electrolyte: the two electrochemical reactions must either share a common electrolyte or use two separate electrolytes that are compatible and can be well-mixed without interfering with each other. Second, the electrodes: both electrodes must be stable in air, compatible with each other, and non-reactive under operational conditions, allowing for the construction of microelectrodes using various fabrication techniques.

Third, the electrochemical window: both reactions must be able to operate stably within the same electrochemical window without mutual interference. Ideally, the redox reaction sites should be distinct, with sequential reactions being the most favorable. This allows for the straightforward verification of the successful integration of the double-reaction system through direct analysis of cyclic voltammetry or charge/discharge profiles. Fourth, the reaction environment: the electrochemical conditions for both reactions, including solution concentration, pH, and reaction temperature, should be either identical or closely aligned. Fifth, the reaction products: the products generated by the first reaction must not interfere with or degrade the second reaction, and vice versa. Ideally, the products of the first reaction should enhance the conductivity of the second reaction system, thereby improving its overall capacity. Achieving such a design will be optimal, but it also poses significant challenges in terms of materials compatibility and reaction dynamics.

Bismuth oxide (Bi₂O₃), due to its low cost and non-toxicity, has been widely studied in photocatalysis³³. More recently, it has been explored in electrochemical systems: as an additive to Zn negative electrodes, Bi₂O₃ improves cycling stability by enhancing conductivity and suppressing hydrogen evolution^{34–36}, while Bi and Bi₂O₃ have also been employed as negative electrodes in various supercapacitors and batteries^{37–43}. Notably, Bi₂O₃ has been utilized as a positive electrode material in aqueous Zn-based batteries^{43–46}, where it delivers promising electrochemical performance. When coupled with Ni foam, Bi₂O₃ exhibits excellent mass and areal capacities⁴³, underscoring its potential as a high-performance electrode material. The reversible conversion between Bi₂O₃ and Bi involves the transfer of up to six electrons, enabling high theoretical capacity and rendering it attractive for next-generation batteries. Unlike conventional batteries, which can employ porous metallic current collectors to maintain conductivity at high active material loadings, MBs must simultaneously address microfabrication constraints, limited material loading at the microscale, and the integration of two distinct microelectrodes on a single substrate^{4,32}. Another key limitation lies in the intrinsically poor conductivity of Bi₂O₃, which makes it difficult to achieve high areal capacity and energy density in Zn||Bi₂O₃ MBs simply by increasing the material loading. In contrast, while pure silver oxide (Ag₂O) electrodes also exhibit limited conductivity, the conversion product, silver, serves as an excellent conductive agent, offering a potential solution to overcome the electrochemical performance limitations associated with Bi₂O₃.

Herein, based on the principles for constructing MBs with dual-cell reactions discussed above, we propose an in situ conductivity enhancement-assisted double-cell reaction strategy to construct high-performance Zn||Bi₂O₃@Ag₂O MBs that integrate the two conversion reactions of Bi₂O₃ and Ag₂O within a single microdevice. This strategy significantly reduces the reliance on inactive battery materials such as substrates and packaging materials, substantially enhancing the space efficiency of the micro-battery. Notably, in the first conversion reaction, Ag₂O with relatively low conductivity is converted into highly conductive metallic silver. Simultaneously, the Bi₂O₃@Ag₂O composite is transformed into Bi₂O₃@Ag, with metallic silver tightly surrounding Bi₂O₃, leading to a substantial increase in the conductivity of the composite. Unlike simply combining Zn||Ag₂O and Zn||Bi₂O₃ MBs, during the second conversion reaction in the Zn||Bi₂O₃@Ag₂O MBs, the in situ conductivity enhancement induced by the Ag₂O conversion reaction achieves a nearly order-of-magnitude increase in the capacity contribution of Bi₂O₃, compared to pure Zn||Bi₂O₃ MBs at the same current density. Moreover, the total capacity of Zn||Bi₂O₃@Ag₂O-based MBs exceeds above 2.1 times of the combined discharge capacities of the individual Zn||Bi₂O₃ and Zn||Ag₂O MBs. Consequently, the constructed microdevice delivers a high areal capacity of 16,561.5 $\mu\text{Ah cm}^{-2}$ at a high current density of 12 mA cm^{-2} . Even at the current density of 30 mA cm^{-2} , the microdevice retains the

crystalline Bi_2O_3 electrode materials are synthesized using a straightforward precipitation method at room temperature (Fig. S1). Flexible graphite paper, known for its excellent conductivity, is precisely patterned into interdigital microelectrodes within seconds using laser etching technology based on a pre-designed pattern (Figs. 1b and S2). Next, the interdigital negative electrode and positive electrode are prepared by applying inks containing zinc powder, Bi_2O_3 , Ag_2O , polyvinylidene fluoride, super P, and N-methyl-pyrrolidone onto the graphite-based microelectrodes. The $\text{Bi}_2\text{O}_3@Ag_2O$ positive electrode and Zn negative electrode on graphite paper are carefully aligned on a customized stainless-steel template attached to polyethylene terephthalate (PET) tape (Fig. 1b). After the template is removed, the PET-supported $Zn||Bi_2O_3@Ag_2O$ microelectrodes are obtained (Fig. 1b). Notably, the zinc powder selected for the negative electrode features a spherical micro-morphology (Fig. S3).

As shown in Fig. S4, a single interdigital microelectrode is remarkably small. By taking advantage of the fabrication strategy combining high-resolution laser direct writing and template method, six microelectrodes can be easily integrated onto a flexible PET tape, which can be wrapped around the wrist and bent into various shapes (Fig. S4). Scanning electron microscopy (SEM) and elemental mapping images show that the $\text{Bi}_2\text{O}_3@Ag_2O$ positive electrode and Zn negative electrode are evenly and alternately integrated (Fig. S5). Notably, as PET contains abundant oxygen, elemental mapping of O across the entire microelectrode cannot accurately delineate the electrode outline. To more clearly define the electrode geometry, elemental maps of Zn, Bi, and Ag, present in the negative electrode and positive electrode but absent from the substrate, are presented in Fig. S5. In Fig. S6, silver oxide presents a morphology of interconnected nanospheres with smooth surfaces. Notably, the synthesized Bi_2O_3 powder appears yellow (Fig. S1), and its X-ray diffraction (XRD) pattern matches well with $\alpha\text{-Bi}_2\text{O}_3$ (PDF# 71-0465, monoclinic) (Fig. S7). The Bi_2O_3 forms microrods resembling wheat-like structures (Fig. S6). Transmission electron microscopy (TEM) further confirms the microrods structure, showing a lattice spacing of approximately 0.322 nm (Fig. S8). Notably, the synthesized Bi_2O_3 exhibits enhanced conductivity and reduced size compared to the commercial counterpart (Figs. S6 and S9). The TEM image of Ag_2O similarly displays interconnected nanospheres, with a lattice spacing of approximately 0.270 nm (Fig. S10). Considering the well-established use of commercial Ag_2O in high-performance $Zn||Ag_2O$ batteries^{47,48}, we employed commercial Ag_2O in this study. Moreover, XRD analysis of the $\text{Bi}_2\text{O}_3@Ag_2O$ positive electrode, in comparison with the PDF standard card, verifies the successful incorporation of both Ag_2O and Bi_2O_3 (Fig. S11).

Capacity enhancement mechanism of the in-situ conductivity enhancement-assisted double-cell reaction strategy

Then, a polyvinyl alcohol/KOH/zinc acetate gel electrolyte with high ionic conductivity is synthesized to enable efficient ion transport (Fig. S12). Thanks to its strong adhesive properties (Fig. S13), this electrolyte integrates seamlessly with various microelectrodes, facilitating the construction of $Zn||Bi_2O_3$, $Zn||Ag_2O$, and $Zn||Bi_2O_3@Ag_2O$ -based MBs. As illustrated in Fig. 2a–c, the cyclic voltammetry (CV) and galvanostatic charge/discharge (GCD) profiles of $Zn||Bi_2O_3$ MBs reveal a pair of redox peaks corresponding to the conversion between Bi_2O_3 and Bi. Although this reaction involves a six-electron transfer, the discharge capacity only reaches $614.4 \mu\text{Ah cm}^{-2}$ at 18 mA cm^{-2} (Fig. 2c), suggesting that the full potential of the six-electron reaction is not fully realized, likely due to the limited electronic conductivity of Bi_2O_3 (Fig. 2d). In parallel, $Zn||Ag_2O$ MBs are assembled and their electrochemical performance is evaluated in Fig. S12. While this microdevice can achieve a high capacity nearing $4671 \mu\text{Ah cm}^{-2}$ at 18 mA cm^{-2} (Fig. S14), significant performance improvements remain challenging due to limitations inherent in the single-cell reaction. To overcome these limitations, $Zn||$

$\text{Bi}_2\text{O}_3@Ag_2O$ -based MBs featuring a double-cell reaction, are constructed (Fig. 2e). The CV curves for these microdevices exhibit two distinct pairs of redox peaks (Fig. 2f), corresponding to the Bi/ Bi_2O_3 and Ag/ Ag_2O transformations. Notably, a pronounced Ag_2O oxidation peak appears at 1.8 V, with no detectable oxygen evolution signal even beyond 2 V, confirming the absence of water decomposition within this voltage window. This configuration delivers two flat discharge plateaus and achieves a remarkable areal capacity of $11393.8 \mu\text{Ah cm}^{-2}$ at 18 mA cm^{-2} (Fig. 2j), comparable to the capacities of $Zn||Bi_2O_3$ and $Zn||Ag_2O$ MBs (Fig. S15). Importantly, the electrochemical process involves only the reversible conversion reactions of $\text{Ag}_2\text{O}/Ag$ and $\text{Bi}_2\text{O}_3/Bi$, with no side reactions between Ag_2O and Bi_2O_3 or their discharge products (Figs. S11 and S16). The capacity contribution of Ag_2O in $Zn||Bi_2O_3@Ag_2O$ MBs closely aligns with that of pure $Zn||Ag_2O$ MBs. Notably, the Bi_2O_3 contribution in $Zn||Bi_2O_3@Ag_2O$ MBs reaches $6597.1 \mu\text{Ah cm}^{-2}$, more than 10.7 times that of $Zn||Bi_2O_3$ MBs alone (Figs. 2d and S17). Furthermore, the total areal capacity and energy density of $Zn||Bi_2O_3@Ag_2O$ MBs exceeds 2.1-fold of the combined value of the two individual MBs (Fig. S18). For the $Zn||Bi_2O_3@Ag_2O$ MBs, the Bi_2O_3 mass loading is approximately 3.6 mg, yielding a theoretical discharge capacity of 1.24 mAh, corresponding to a theoretical specific capacity of 345 mAh g^{-1} (Fig. S19). Benefiting from the in situ conductivity enhancement provided by Ag generated from Ag_2O during the discharging process, the Bi_2O_3 component in $Zn||Bi_2O_3@Ag_2O$ MBs delivers 1.18 mAh (328 mAh g^{-1}) even at high areal loading of 40 mg cm^{-2} (Fig. S19a), achieving ~95% of the theoretical specific capacity. In contrast, without Ag_2O , Bi_2O_3 exhibits a measured capacity of only 0.128 mAh (35.5 mAh g^{-1}) under the same loading (Fig. S19b), corresponding to merely 10.3% of the theoretical value. These results demonstrate that the in situ conductivity enhancement-assisted double-cell reaction strategy enabled by Ag_2O incorporation is crucial for boosting the capacity of Bi_2O_3 by an order of magnitude even under high loading, thereby enabling the $Zn||Bi_2O_3@Ag_2O$ MBs to achieve high areal/mass capacity and energy density. Notably, as the Bi_2O_3 mass loading increases, conventional conductive agents alone cannot effectively improve internal electron transport within the electrode (Fig. S20a), explaining the low discharge capacity observed in pure $Zn||Bi_2O_3$ MBs containing Super P. To explore the underlying enhancement, we examine the reaction mechanism in the $Zn||Bi_2O_3@Ag_2O$ -based MBs (Fig. 2d). By incorporating the Ag_2O electrode into the Bi_2O_3 system, the Ag produced during the first discharge reaction effectively surrounds the Bi_2O_3 (Figs. 4 and 5 for further details). This not only mitigates the inherent conductivity limitations of Bi_2O_3 but also facilitates the utilization of the six-electron transfer reaction, thereby enhancing the overall reaction kinetics (Figs. 2d and S20b). To verify this mechanism, we prepared Bi_2O_3 , $\text{Bi}_2\text{O}_3@Ag_2O$, and $\text{Bi}_2\text{O}_3@Ag$ microelectrodes with the same electrode loading as used in MB measurements (Fig. S21), rather than directly coating Bi_2O_3 , $\text{Bi}_2\text{O}_3@Ag_2O$, and $\text{Bi}_2\text{O}_3@Ag$ onto graphite paper without matching the loading to that of the microelectrodes. The resistance measurements of the microelectrodes show that incorporating Ag into Bi_2O_3 significantly reduces electrode resistance compared with both pure Bi_2O_3 and $\text{Bi}_2\text{O}_3@Ag_2O$ (Fig. S21), further confirming that Ag enhances conductivity and then electrochemical performance. Additionally, the electrical resistance, resistivity, and conductivity of Bi_2O_3 , $\text{Bi}_2\text{O}_3@Ag_2O$, and $\text{Bi}_2\text{O}_3@Ag$ composites are further measured by four-probe instrument (Fig. S22), revealing that the $\text{Bi}_2\text{O}_3@Ag$ composite exhibits the highest conductivity, along with the lowest resistance and resistivity.

Further validation is obtained through ex situ electrochemical impedance spectroscopy (EIS) on $Zn||Bi_2O_3@Ag_2O$ MBs (Figs. 2h and S23). When the discharge voltage reaches -1.2 V (as $\text{Bi}_2\text{O}_3@Ag_2O$ transitions to $\text{Bi}_2\text{O}_3@Ag$), the charge-transfer resistance (R_{ct}) of $Zn||Bi_2O_3@Ag_2O$ MBs declines from 16 to 9.8Ω . With further discharge to 0.2 V ($\text{Bi}_2\text{O}_3@Ag$ converts to $Bi@Ag$), R_{ct} decreases

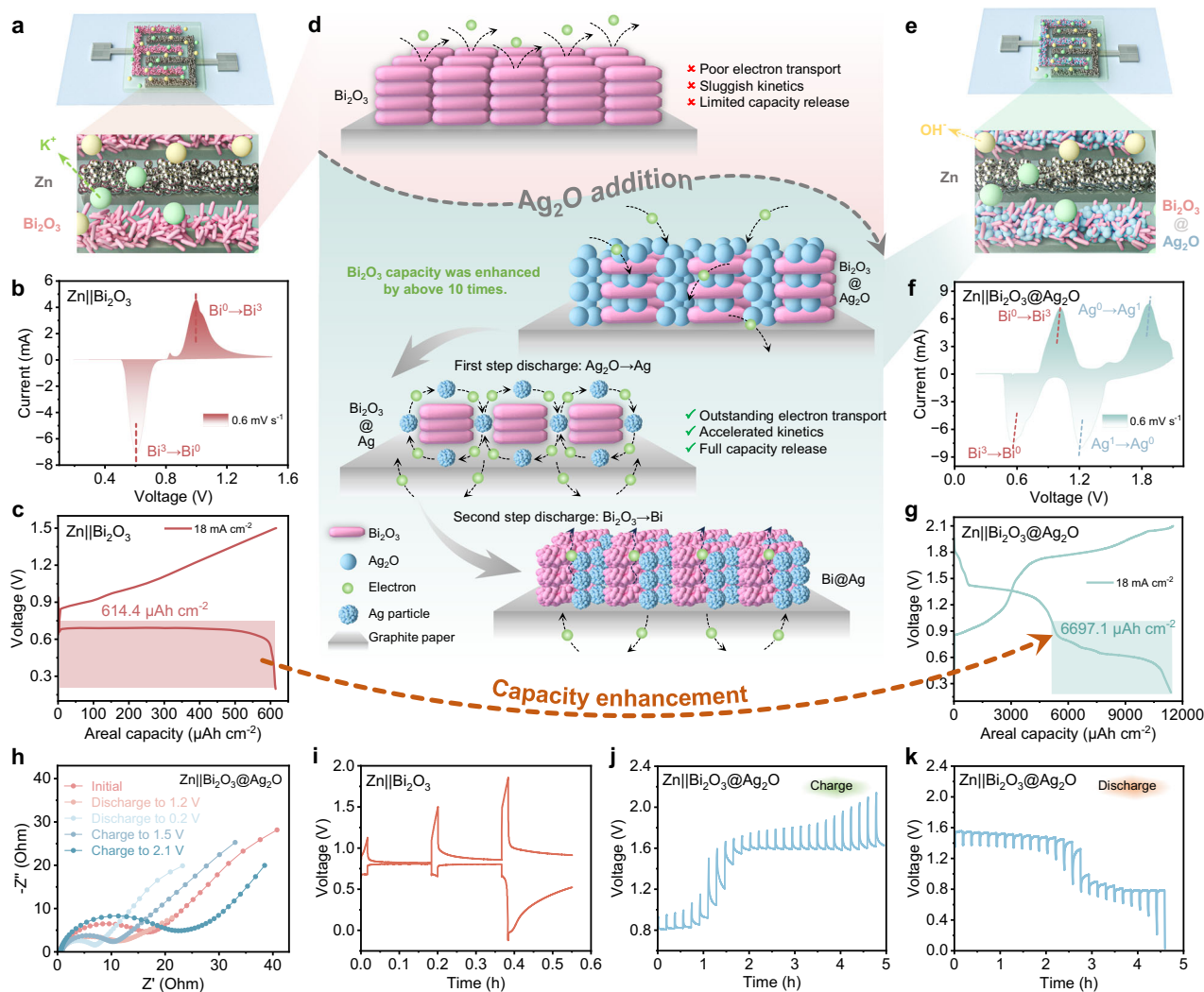


Fig. 2 | The capacity enhancement mechanism of the in situ conductivity enhancement-assisted double-cell reaction strategy. **a** The schematic diagram, **b** CV curves at 0.6 mV s⁻¹ and **c** GCD profiles at 18 mA cm⁻² of Zn||Bi₂O₃ MBs. **d** Schematic diagram of the mechanism of conductivity enhancement of Bi₂O₃@Ag₂O composite. **e** The schematic diagram, **f** CV curves at 0.6 mV s⁻¹ and **g**

GCD profiles at 18 mA cm⁻² of Zn||Bi₂O₃@Ag₂O MBs. **h** The ex-situ EIS curves under different charging and discharging conditions of Zn||Bi₂O₃@Ag₂O batteries. **i** GITT curves of pure Zn||Bi₂O₃ MBs. The GITT curve and the calculated diffusion coefficients during **j** charging and **k** discharging processes of Zn||Bi₂O₃@Ag₂O MBs.

further to -6Ω (Fig. S23). Upon charging from 0.2 to 1.5 V (Bi@Ag reverts to Bi₂O₃@Ag), resistance increases modestly but remains lower than when charged to 2.1 V (Bi₂O₃@Ag returns to Bi₂O₃@Ag₂O). These reversible EIS changes support the conclusion that the high conductivity of Ag generated in the initial step is crucial for maximizing capacity in the second step (Figs. 2h and S23). Additionally, we conduct galvanostatic intermittent titration technique (GITT) measurements to analyze the reaction kinetics in Zn||Bi₂O₃ and Zn||Bi₂O₃@Ag₂O MBs (Figs. 2i–k and S24). In Fig. 2i, the GITT curves of pure Zn||Bi₂O₃ MBs reveal only three relaxation cycles during both charge and discharge, with a discharge duration of ~ 0.5 h. This microdevice also exhibits pronounced polarization and a slow relaxation recovery rate, primarily due to the high mass loading that impedes electron transport within the Bi₂O₃ (Fig. S25). In contrast, Zn||Bi₂O₃@Ag₂O MBs display well-defined GITT curves with a discharge duration of ~ 4.5 h, of which ~ 2 h originates from the Bi₂O₃ (Fig. 2j, k), which is substantially longer than that in pure Zn||Bi₂O₃ MBs. Similarly, compared to pure Zn||Bi₂O₃ MBs, Zn||Bi₂O₃@Ag₂O MBs show a lower polarization and better relaxation recovery (Figs. 2i–k and S18), which can be attributed to the in situ formation of Ag during the initial cycles creates percolating

conductive networks that enhance electron transport within the thick Bi₂O₃ electrode (Fig. S25), thereby improving kinetic performance. These findings provide further evidence for the enhanced capacity of Bi₂O₃ in the Zn||Bi₂O₃@Ag₂O MBs, validating our proposed mechanism.

The electrochemical performance of Zn||Bi₂O₃@Ag₂O MBs

Figure 3a illustrates the reaction mechanism during the charge/discharge process of Zn||Bi₂O₃@Ag₂O MBs. The first and second steps represent the conversion reactions of Ag₂O to Ag and Bi₂O₃ to Bi, respectively. Various gel electrolytes with different concentrations are used to optimize the microdevice (Fig. S26), with the PVA/3 m KOH/zinc acetate gel electrolyte emerging as the optimal candidate due to its higher ionic conductivity (Fig. S27). Notably, the optimum mass ratio of Ag₂O to Bi₂O₃ in Zn||Bi₂O₃@Ag₂O MBs is 2:1 (Fig. S28). At a current density of 12 mA cm⁻², the fabricated Zn||Bi₂O₃@Ag₂O MBs deliver a maximum areal capacity of 16,561.5 μ Ah cm⁻² (Fig. 3b, c). Even at a high current density of 20 mA cm⁻² and 30 mA cm⁻², these micro-devices achieve a high areal capacity of 9602.02 μ Ah cm⁻² and 4406.12 μ Ah cm⁻², respectively, demonstrating high-rate performance.

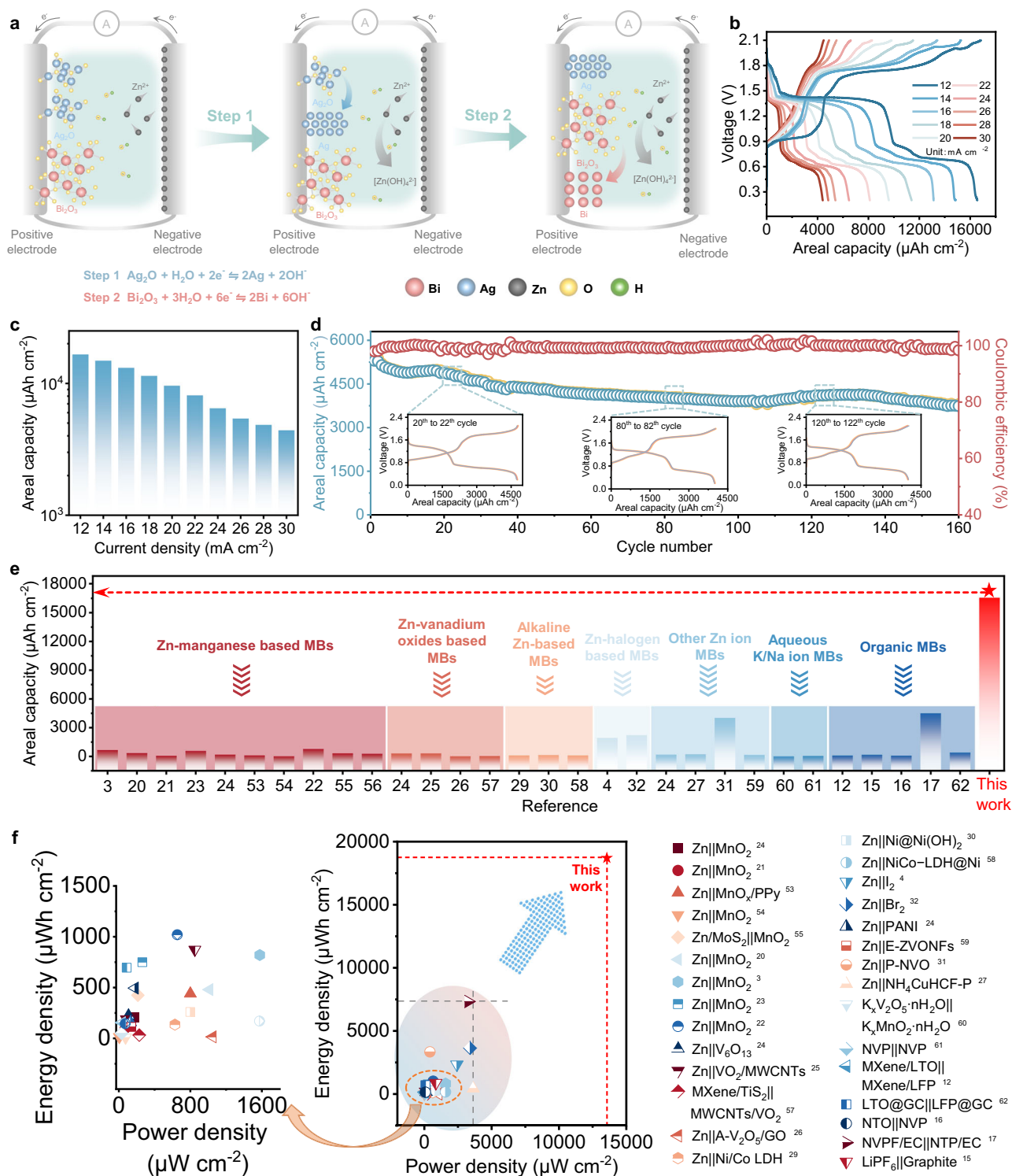


Fig. 3 | Electrochemical performance of Zn||Bi₂O₃@Ag₂O MBs. a The Schematic diagram of structure reaction mechanism, **b** GCD curves **c** Areal capacity under the different current density, **d** Cycle performance of Zn||Bi₂O₃@Ag₂O MBs. **e** The comparison of the areal capacity of the constructed Zn||Bi₂O₃@Ag₂O MBs with that of all reported aqueous Zn-based MBs, including Zn-manganese based MBs^{3,20–24,53–56}, Zn-vanadium oxides based MBs^{24–26,57}, alkaline zinc-based MBs^{29,30,58},

Zn-halogen based MBs^{4,32} and other Zn ion MBs^{24,27,31,59} as well as state-of-the-art aqueous K/Na ion MBs^{60,61}, and organic MBs including Li ion MBs^{12,62}, Na ion MBs^{16,17} and dual-ions MBs¹⁵. **f** The comparison of maximum areal energy density and its corresponding power density of the constructed microdevice with that of all reported aqueous Zn-based MBs^{3,4,20–27,29–32,53–59}, state-of-the-art aqueous K/Na ion MBs^{60,61}, and organic MBs^{12,15–17,62}.

Due to the in situ conductivity enhancement-assisted double-cell reaction mechanism, these capacities significantly exceed those of Zn||Bi₂O₃ MBs (Fig. S29a, b). Furthermore, the Bi₂O₃ capacity contribution in Zn||Bi₂O₃@Ag₂O MBs ranges from 7131 $\mu\text{Ah cm}^{-2}$ at 12 mA cm^{-2} to

3473.8 $\mu\text{Ah cm}^{-2}$ at 30 mA cm^{-2} , representing nearly an order of magnitude increase than that of pure Zn||Bi₂O₃ MBs at the same current density (Fig. S29c). This enhanced performance arises from the high conductivity of Ag generated during the first-step discharge in the Zn||

Ag₂O battery, which markedly improves the conductivity of the Zn||Bi₂O₃ system in the second step, thereby boosting capacity. After 160 cycles, the Zn||Bi₂O₃@Ag₂O MBs can deliver a high areal capacity of 3741.6 μAh cm⁻², corresponding to 70.1% of the initial value (Fig. 3d). The inflection points of GCD curves are different for the three cycle points in Fig. 3d, which can be attributed to the dynamic evolution of the composite electrode materials during cycling. Initially, the mass loading of Ag₂O is approximately twice that of Bi₂O₃, and complete penetration and interaction with the electrolyte occur gradually, resulting in a progressive activation process. In the second stage, Ag₂O reaches peak electrochemical activity, undergoing nearly complete transformation; however, this extensive reaction limits electrolyte access to portions of Bi₂O₃, slightly reducing its capacity contribution. In the third stage, excessive Ag₂O consumption in the alkaline electrolyte leads to a decline in its capacity contribution (Fig. S30), while previously isolated Bi₂O₃ regions gain electrolyte access and become electrochemically active, causing a moderate capacity increase relative to the second stage. Beyond 160 cycles, up to 255 cycles, the Bi₂O₃ contribution remains stable (Fig. S30), in agreement with SEM, XRD, and TEM results showing minimal structural change (Fig. S30). In contrast, Ag₂O exhibits pronounced morphological and structural depletion after 160 cycles (Fig. S30), resulting in a markedly reduced capacity contribution compared with the initial stage. Notably, similar capacity attenuation is common in previously reported Zn||Ag₂O batteries, whose cycle life is typically limited to ~120 cycles^{47,49–51}. Furthermore, the corrosion of the zinc negative electrode in alkaline electrolytes is an inherent phenomenon in alkaline zinc-based batteries and represents a key factor on capacity decay during prolonged cycling⁵². Based on the cycling curves of Zn||Bi₂O₃@Ag₂O MBs, the average Ag/Ag₂O conversion rate is estimated at ~94.1% (Fig. S31), underscoring the good reversibility of the electrochemical reactions during cycling. Due to the reasonable structural designs, a high areal capacity of 16,561.5 μAh cm⁻² of the Zn||Bi₂O₃@Ag₂O MBs is obtained at 12 mA cm⁻², competitive with all reported aqueous Zn-based MBs, including Zn-manganese based MBs^{3,20–24,53–56}, Zn-vanadium oxides based MBs^{24–26,57}, alkaline zinc-based MBs^{29,30,58}, Zn-halogen based MBs^{4,32} and other Zn-ion MBs^{24,27,31,59} as well as state-of-the-art aqueous K/Na ion MBs^{60,61}, and organic MBs including Li ion MBs^{12,62}, Na ion MBs^{16,17} and dual-ions MBs¹⁵ (Fig. 3e and Table S1). Unlike other aqueous zinc-based MBs, which typically reach maximum areal capacity below 2 mA cm⁻², only a few exceed 2 mA cm⁻² (Fig. S32). Operating at such high current densities also avoids the water-related side reactions under high voltage. Owing to its optimized design, the Zn||Bi₂O₃@Ag₂O MBs reach maximum areal power density, significantly higher than all reported Zn-based micro-batteries^{3,4,20–27,29–32,53–59} (Fig. S33). This ability to withstand high current density enables the microdevices to deliver a high areal energy density of ~19,000 μWh cm⁻² even at a high-power density of ~13,550 μW cm⁻², comparable to the best available aqueous Zn-based MBs (Fig. 3f and Table S1)^{3,4,20–27,29–32,53–59}. Even when compared with the reported top-performing organic MBs, the areal energy density of our microdevices is at least 2.5 times higher (Fig. 3f and Table S1)^{12,15–17,62}. Notably, even when the inactive gap area is included in the calculations, the maximum areal capacity and energy density of our Zn||Bi₂O₃@Ag₂O MBs still surpass those of all previously reported high-performance MBs (Fig. S34). When the energy density decreases to 3410.43 μWh cm⁻², a high power density of 23,231.8 μW cm⁻² is achieved, comparable to MSCs^{63–70} and state-of-the-art Zn or Li ion MSCs including Zn||activated carbon MSCs (≤3900 μW cm⁻²)^{71,72}, Zn||CNT MSCs (8000 μW cm⁻²)⁷³, Zn ion micro-capacitors with activated carbon negative electrode and VO₂ (B) positive electrode (753.12 μW cm⁻²)⁷⁴, Zn||MXene/silver-nano-wires MSCs (≤4500 μW cm⁻²)^{75,76}, Li ion MSCs (<2990 μW cm⁻²)⁷⁷, and Na ion MSCs (900 μW cm⁻²)⁷⁸ (Fig. S35 and Table S2). Volumetrically, when accounting for the combined thickness of the positive electrode, negative electrode, and graphite paper current collector (Fig. S36), the

microdevice achieves a maximum volumetric energy density of 393.8 mWh cm⁻³ at a power density of 285.4 mW cm⁻³. This performance surpasses that of most of the reported high-performance Zn-based MBs^{53–58}, organic Li/Na/double ions MBs^{14–16} and other aqueous MBs⁶¹, offering more than 50- and 500-fold improvements in energy density over Li thin-film batteries (4 V/500 μAh)⁷⁹ and commercial supercapacitors (5.5 V/100 mF and 2.75 V/44 mF)⁸⁰, respectively (Fig. S36). Moreover, compared with most fiber-shaped MBs, Zn||Bi₂O₃@Ag₂O MBs exhibit both higher volumetric capacity and superior energy density (Fig. S37). Even after 12 h of rest in a fully charged state, the fabricated MBs can still deliver a high areal capacity at a high current density of 18 mA cm⁻², competitive with that of other reported high-performance aqueous Zn-based MBs without resting (Fig. S38). Notably, the electrochemical performance of our MBs, specifically areal capacity and areal energy, is compared with the reported MBs under conditions where the total microelectrode area, including both the positive and negative electrode is comparable (Fig. S39). As a summary, the high electrochemical performance of the Zn||Bi₂O₃@Ag₂O MBs can be attributed to several critical factors. First, the PVA/KOH/zinc acetate gel electrolytes with high ion conductivity provide sufficient ions for continuous redox reactions within the Zn||Bi₂O₃@Ag₂O MBs. Second, combining two battery reactions within a single microdevice maximizes space utilization without increasing inactive areas, significantly enhancing discharge capacity and energy density. Third, incorporating Ag₂O markedly improves the reaction kinetics and discharge capacity of Bi₂O₃, delivering nearly a tenfold increase over Zn||Bi₂O₃ MBs. This improvement is due to the conductive Ag generated during the initial conversion step, which establishes an effective electron-conducting pathway between Bi₂O₃ and the graphite paper current collector, thereby facilitating the six-electron Bi₂O₃ conversion reaction. Furthermore, the correlation between the peak current density (*i_p*) of both the anodic and cathodic reactions versus the square roots of scan rates (*v*^{1/2}) is obtained in Fig. S39, derived from CV curves of each electrochemically active species under different scan rates. The result shows that the plots of *i_p* vs. *v*^{1/2} is a linear relationship, confirming that redox reaction in our fabricated Zn||Bi₂O₃@Ag₂O MBs is mainly diffusion-controlled (Fig. S40)^{81,82}. Based on the established method for determining *b* values from CV curves^{83,84}, both reduction peaks exhibit *b* values close to 0.5 (Fig. S40), further verifying that the charge-storage process of our MBs are almost entirely governed by ion diffusion-controlled battery behavior. Lastly, the well-designed structure supports the reversible and stable electrochemical reactions of zinc with both Ag₂O and Bi₂O₃, ensuring the sustained high performance of these MBs.

The reaction mechanism of batteries

The working mechanism of Zn||Bi₂O₃@Ag₂O MBs is investigated in Fig. 4a–e. As the discharge voltage decreases, the large, smooth Ag₂O spheres in the Bi₂O₃@Ag₂O composite first convert into small, rough Ag particles, while the morphology of Bi₂O₃ remains essentially unchanged (Fig. 4a, b). Notably, during this process, the smooth Bi₂O₃ microrods become encased in the highly conductive Ag particles formed from Ag₂O, which significantly enhances the conductivity of the entire composite. This enhancement explains the substantially higher capacity contribution of Bi₂O₃ in the Zn||Bi₂O₃@Ag₂O system compared to that of pure Zn||Bi₂O₃ MBs. As the discharge voltage further drops to 0.2 V, the smooth Bi₂O₃ microrods transform into rough, hollow Bi, while the rough Ag particles remain unchanged (Fig. 4c). Upon recharging to a fully charged state, the Bi@Ag composite first reverts to Bi₂O₃@Ag (Fig. 4d) and then to Bi₂O₃@Ag₂O (Fig. 4e). Notably, upon completion of battery discharge, the microrod structure of Bi₂O₃ was almost entirely lost in Fig. 4c. As charging proceeded, this micro-rod morphology gradually re-emerged (Fig. 4d, e). Compared with the vanished structure observed in Fig. 4c, the pronounced microrod features in Fig. 4d, e clearly demonstrate the

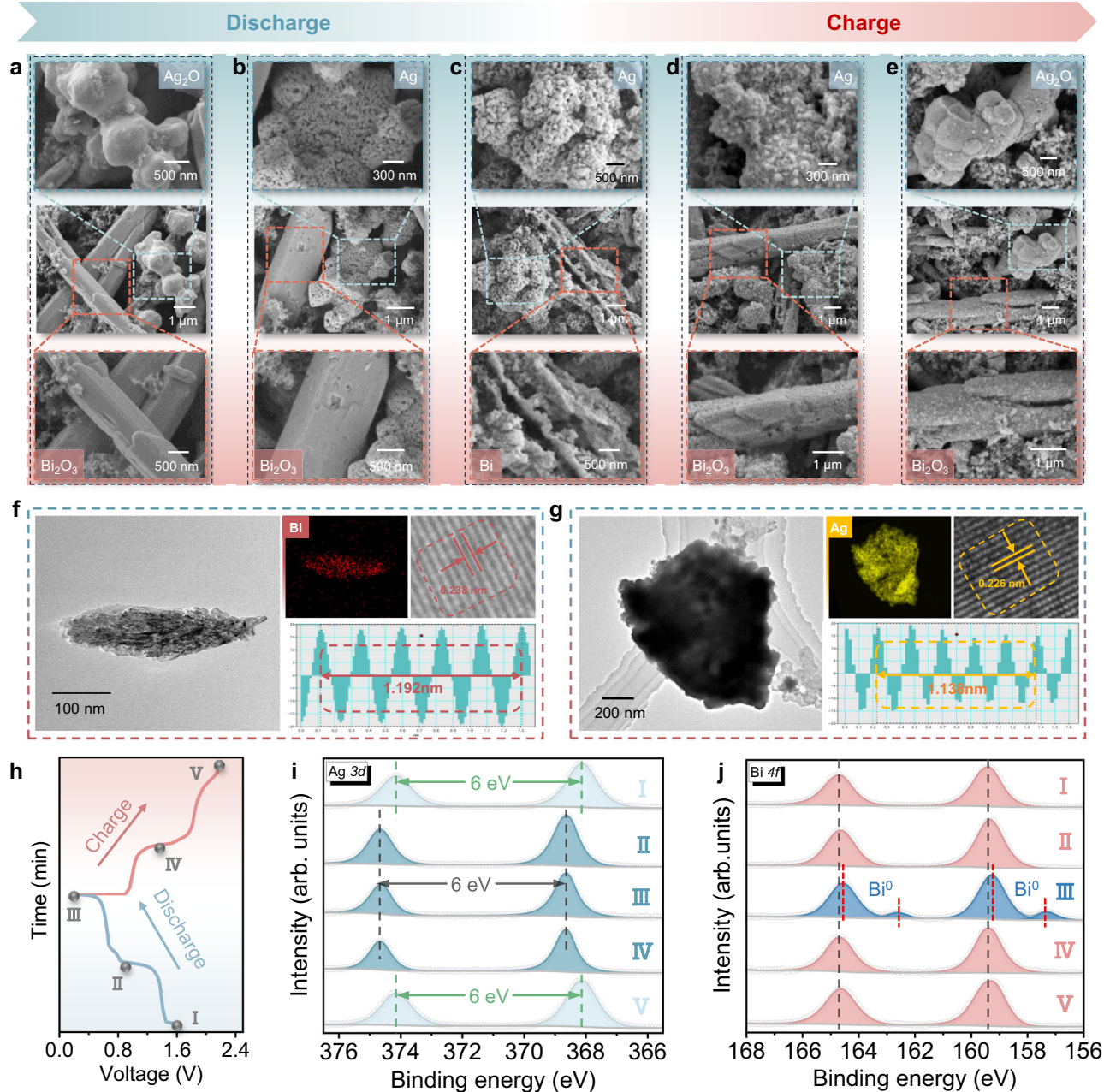


Fig. 4 | Ex situ testing and analysis. **a–e** The ex situ SEM images of the positive electrodes of Zn||Bi₂O₃@Ag₂O MBs under the different discharging and charging stages at 0.5 A g⁻¹. The TEM images and corresponding element mapping of **f** Bi and

g Ag under the fully discharged state at 0.5 A g⁻¹. **h** The discharging and charging curves and corresponding ex situ XPS curves of **i** Ag 3d and **j** Bi 4f of Zn||Bi₂O₃@Ag₂O MBs at 0.5 A g⁻¹.

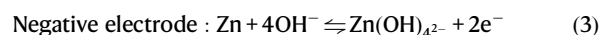
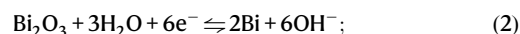
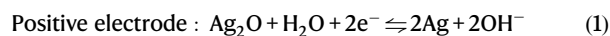
regeneration of Bi₂O₃, demonstrating the reversibility of the entire charge–discharge process. Furthermore, TEM images of the fully discharged state reveal that the produced Bi and Ag exhibit distinctly different morphologies from the smooth Bi₂O₃ microrods and interconnected smooth Ag₂O nanospheres (Figs. 4f, g, S8 and S10). Ex situ X-ray photoelectron spectroscopy (XPS) analysis further investigates the changes in Bi₂O₃ and Ag₂O across various charge and discharge states (Fig. 4h, i). From the initial state (I) to stage II of discharge (Fig. 4h), the Ag 3d peaks shift upward, while the Bi 4f peaks remain stable, indicating the transformation of Bi₂O₃@Ag₂O to Bi₂O₃@Ag. With further discharge to stage III, the Bi₂O₃ peak shifts downward, and a new peak appears (Fig. 4j), closely aligning with the XPS peak of commercial pure Bi powder (Fig. S41), indicating the complete conversion of Bi₂O₃ to Bi. Throughout this stage, the Ag 3d peak remains

essentially unchanged, functioning primarily as a conductivity enhancer. Thus, between stages II and III, Bi₂O₃@Ag₂O is transformed into Bi@Ag. As charging proceeds from the fully discharged state (III) to stages IV and V (fully charged state), the Ag 3d and Bi 4f peaks gradually revert to their original positions and shapes (Fig. 4h–j), corresponding to the transformation from Bi@Ag back to Bi₂O₃@Ag and ultimately to Bi₂O₃@Ag₂O, respectively.

Moreover, the ex-situ fourier transform infrared spectroscopy (FT-IR) was employed to track peak variations of the Bi₂O₃@Ag₂O composite under different charge and discharge states (Fig. S42). At the beginning of discharge, the Bi–O–Bi stretching vibrations between 800 and 900 cm⁻¹ and the Bi–O stretching band at 1390 cm⁻¹ remain largely unchanged, as the initial reaction is dominated by the reduction of Ag₂O to Ag (Fig. S42). In addition, because the characteristic peaks

of Ag_2O and Bi_2O_3 in the $400\text{--}700\text{ cm}^{-1}$ region strongly overlap with the hydroxyl band near 1650 cm^{-1} (arising from surface-adsorbed water of $\text{Ag}_2\text{O}/\text{Bi}_2\text{O}_3$), spectral variations in these regions are also minimal (Fig. S42). As discharge progresses, the Bi-O-Bi stretching vibrations between 800 and 900 cm^{-1} disappear, and the intensity of the Bi-O stretching band at 1390 cm^{-1} decreases significantly (Fig. S42), indicating the reduction of Bi_2O_3 to Bi. By the end of discharge, the peaks corresponding to Ag-O bonds and $[\text{BiO}_6]$ units ($400\text{--}700\text{ cm}^{-1}$), together with the hydroxyl band near 1650 cm^{-1} , also vanish, confirming that both Ag_2O and Bi_2O_3 are reduced to Ag and Bi (Fig. S42). Upon charging, the characteristic peaks of Ag_2O and Bi_2O_3 re-emerge, highlighting the high reversibility of the overall redox process. It is worth noting that although the strong overlap of Bi_2O_3 and Ag_2O peaks obscures direct observation of the $\text{Ag}_2\text{O}/\text{Ag}$ conversion in ex situ FT-IR, this transformation is unambiguously confirmed by ex situ SEM, ex situ XPS analyses and in situ XRD (See Fig. 5). Based on ex situ SEM, TEM, XPS, and FT-IR results, a schematic of the reversible transformation mechanism in $\text{Zn}||\text{Bi}_2\text{O}_3@/\text{Ag}_2\text{O}$ MBs is depicted in Fig. 5a. Meanwhile, the energy-level evolutions during the conversion processes of $\text{Ag}_2\text{O}/\text{Ag}$ and $\text{Bi}_2\text{O}_3/\text{Bi}$ are also studied by density functional theory (DFT) calculations (Fig. S43 and Supplementary Data 1). To gain deeper insights into this reversible reaction mechanism, in situ X-ray diffraction (XRD) analysis was performed to monitor the positive electrode transformations during charge and discharge process (Fig. 5b–i and S44). As seen in Fig. 5b–g, during discharge, specific Bi_2O_3 crystal planes, including (-121) , (-202) , (221) , and (-322) , engage in the reaction. This is confirmed by in situ XRD patterns showing the gradual disappearance of the characteristic peaks of Bi_2O_3 , alongside

the appearance of new peaks at 27.26° (012), 39.6° (101), 45.9° (006), 48.69° (202), 56° (-242), and 62.2° (116) for Bi (a region where the color turns red). Upon charging, these Bi peaks fade, and new peaks at 27.38° , 33.2° , 46.34° , and 52.37° signify the reformation of Bi_2O_3 . Simultaneously, the transformation of Ag_2O was also tracked in situ. At the start of discharge, the Ag_2O characteristic peak at 54.8° (220) gradually diminishes, giving rise to prominent Ag peaks at 38.07° (111) and 64.5° (220). During charging, the Ag peaks recede, and Ag_2O is regenerated. This comprehensive analysis demonstrates that the conversion reactions between $\text{Bi}_2\text{O}_3@/\text{Ag}_2\text{O}$ and $\text{Bi}@/\text{Ag}$ are highly reversible, with the electrode reactions described as follows:



Potential application and wirelessly intelligent integration of the constructed MBs

To visually highlight the high performance of the $\text{Zn}||\text{Bi}_2\text{O}_3@/\text{Ag}_2\text{O}$ MBs, a single microdevice is used to continuously power a timer. Remarkably, a single $\text{Zn}/\text{Bi}_2\text{O}_3@/\text{Ag}_2\text{O}$ MB maintains uninterrupted power to the timer for 3780 minutes (over 2.5 days) without any loss in brightness (Fig. 6a and Supplementary Movie 1). Notably, the mass of

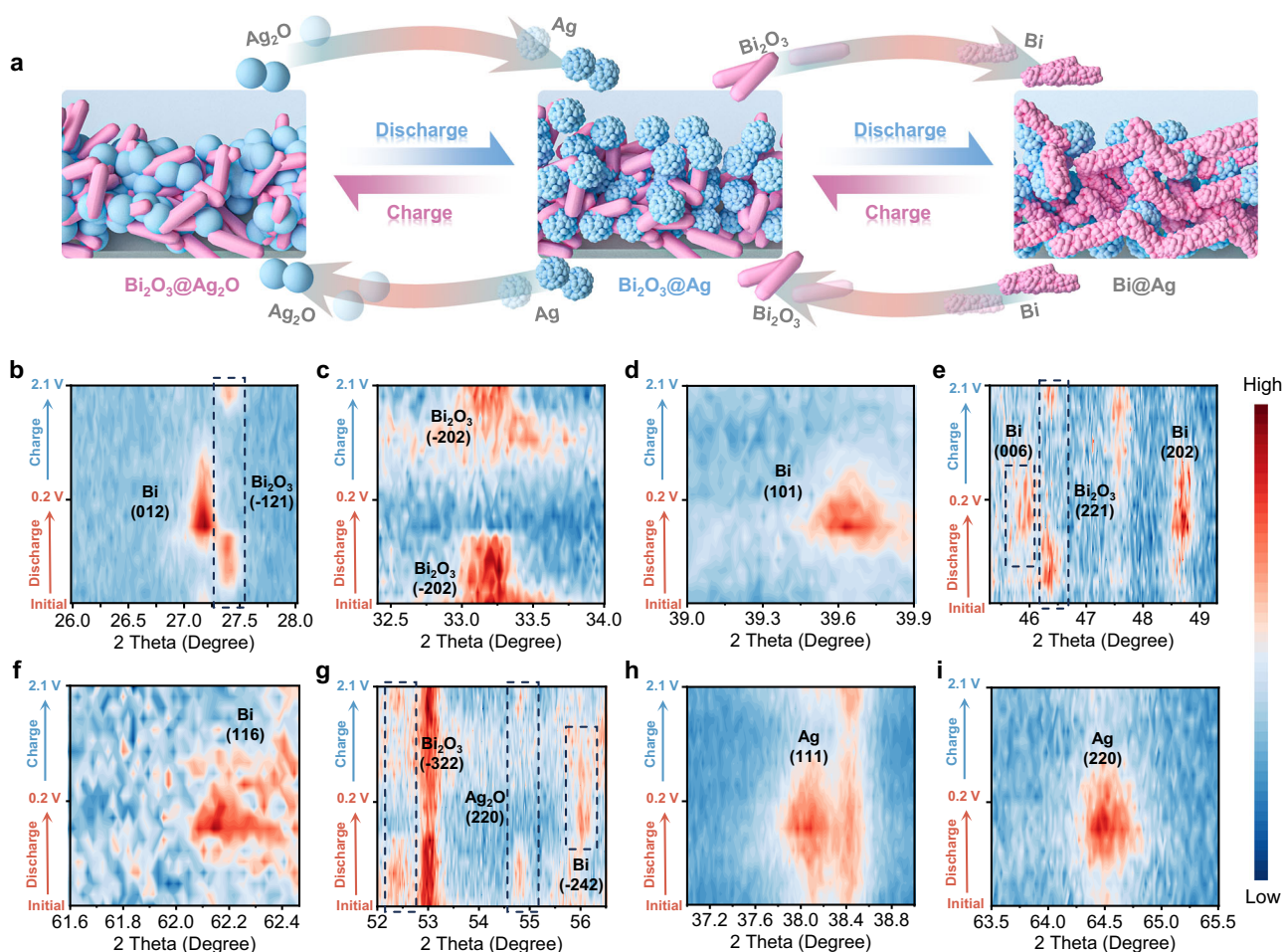


Fig. 5 | Mechanism analysis. **a** Schematic diagram of reaction process of $\text{Zn}||\text{Bi}_2\text{O}_3@/\text{Ag}_2\text{O}$ MBs. **b–i** in situ XRD during charge/discharge of $\text{Zn}||\text{Bi}_2\text{O}_3@/\text{Ag}_2\text{O}$ batteries at 0.2 A g^{-1} .

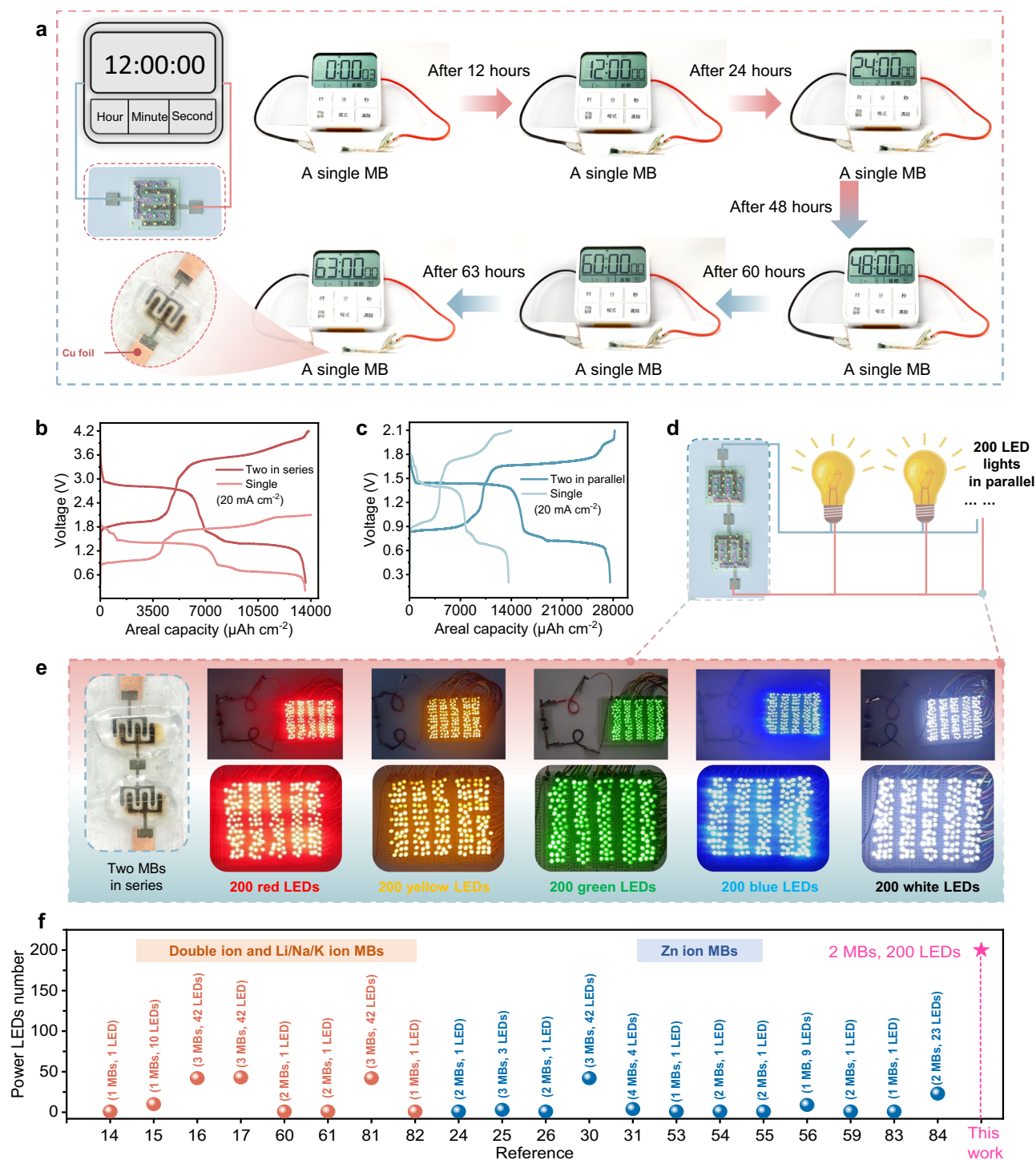


Fig. 6 | Series/parallel testing and the applicability in high-energy-demand scenarios of Zn||Bi₂O₃@Ag₂O MBs. **a** Photograph showing that a single microdevice can uninterrupted power for the timer for over 3780 minutes (over 2.5 days) without any loss in brightness. **b** GCD curves of a single and two Zn||Bi₂O₃@Ag₂O MBs in series and **(c)** in parallel. **d**, **e** Photograph showing that two series-

connected Zn||Bi₂O₃@Ag₂O MBs can easily power 200 red, yellow, green, blue and white light-emitting diodes (LEDs) in parallel. **f** Comparison of the number of LEDs powered by two series-connected Zn||Bi₂O₃@Ag₂O MBs with those powered by other high-performance double ion, Li/Na/K ion MBs^{14-17,60,61,85,86} as well as aqueous Zn-based MBs^{24-26,30,31,53-56,59,87,88}.

the constructed microdevice is 0.44% and 2.4% that of the timer and a commercial battery, respectively (Fig. S45). To meet the increasing demands of integrated circuits, higher voltages and capacities are readily achievable by connecting multiple Zn||Bi₂O₃@Ag₂O MBs in series or parallel. As expected, two Zn||Bi₂O₃@Ag₂O MBs connected in series provide a high platform voltage of ~3 V while retaining a similar areal discharge capacity to a single device (Fig. 6b). Connecting two

MBs in parallel doubles the discharge capacity at the same current density (Fig. 6c). Two series-connected Zn||Bi₂O₃@Ag₂O MBs can power 200 red, yellow, green, blue and white light-emitting diodes (LEDs) in parallel (Fig. 6d, e and Supplementary Movie 2). This LED count is higher than those powered by previously reported microbattery system, including high-voltage and high-performance organic NiSn/LiMnO₂ Li ion MBs (1 MB, 1 red LED)¹⁴, organic dual-ion MBs (1

MB, 10 red or blue or yellow or white LEDs)¹⁵, organic Na ion MBs (3 MBs, 42 yellow LEDs)^{16,17}, aqueous K ion MBs (2 MBs, 1 red LED)⁶⁰, aqueous Na ion MBs (2 MBs, 1 red LED)⁶¹, lithium titanate/lithium iron phosphate Li ion MBs (3 MBs, 42 yellow LEDs)⁸⁵, organic Li||LiFePO₄ MBs (1 MB, 1 white LED)⁸⁶, and the reported advanced aqueous Zn-based MBs^{24–26,30,31,53–56,59,87,88} (Fig. 6f). Moreover, two series-connected microdevices can power white LEDs continuously for approximately 40 minutes (Supplementary Movie 2). To our knowledge, this achievement marks a significant milestone, underscoring the tremendous potential application value of Zn||Bi₂O₃@Ag₂O MBs. When integrated multiple Zn||Bi₂O₃@Ag₂O microelectrodes into an array on a flexible PET substrate, the device demonstrates remarkable flexibility and can be bent to a large degree (Fig. S46). The fabricated Zn||Bi₂O₃@Ag₂O MBs array can stably power a 4.5 V LED under normal conditions, and the LED remains fully operational even when the array is bent into various shapes (Fig. S46 and Supplementary Movie 3). These results highlight the strong potential of our MBs design for developing flexible arrays capable of delivering stable energy output under a wide range of bending conditions.

At present, intelligent wireless sensors are becoming increasingly prevalent in everyday life and work environments. However, these sensors are typically powered by traditional button lithium batteries, which present notable limitations: (1) they require heavy stainless-steel casings, elastic sheets, and gaskets for secure sealing, adding significant weight and volume to the device; (2) they contain flammable organic electrolytes, which pose potential safety hazards. This limitation arises primarily from the high energy demands of Bluetooth transmitters, which are essential for wireless communication with mobile phones, as well as the power required for data processing functions of the sensor. Consequently, developing high-performance aqueous Zn-based MBs capable of powering such wireless sensors remains a challenge. Here, for the first time, we demonstrate the use of aqueous Zn||Bi₂O₃@Ag₂O MBs to power a commercial wireless smart sensor with direct mobile connectivity for monitoring the motion states of toy cars and human bodies (Fig. 7a). As shown in Fig. 7b, c and Supplementary Movie 4, when the Zn||Bi₂O₃@Ag₂O MBs-powered sensor rotates in any of the X, Y, or Z directions, its deflection direction and state can be observed in real time on a mobile phone receiving the wireless signal of sensors. The sensor is then integrated into a toy car, accurately and stably tracking its acceleration and angular velocity during motion and rotation (Fig. 7d, e, Fig. S47 and Supplementary Movie 5). When the car travels over different terrains, such as a smooth plastic track versus uneven grass, the sensor captures distinct acceleration profiles, with greater fluctuation observed on the grass (Fig. 7f and Supplementary Movie 5). Additionally, the sensor can be worn on a person's arm, wirelessly transmitting data to a mobile phone to monitor different motion states in real time, such as walking, standing still, and running (Fig. 7g and Supplementary Movie 6). Collectively, these results demonstrate that our fabricated Zn||Bi₂O₃@Ag₂O MBs with high energy density can be effectively integrated into smart wearable devices, highlighting their promising application potential.

Discussion

We propose a double-cell reaction strategy, assisted by an in situ conductivity enhancement mechanism, to fabricate high-performance Zn||Bi₂O₃@Ag₂O MBs by integrating two conversion reactions within a single microdevice. This approach eliminates the need for additional inactive connecting materials, thereby optimizing the space utilization of MBs. In the first conversion reaction, the Bi₂O₃@Ag₂O composite is transformed into Bi₂O₃@Ag, with metallic silver tightly surrounding the Bi₂O₃, resulting in a substantial increase in the conductivity of the composite. Unlike a simple combination of Zn||Ag₂O and Zn||Bi₂O₃ MBs, the in situ conductivity enhancement induced by the Ag₂O conversion reaction achieve a nearly order-of-magnitude increase in the

capacity contribution of Bi₂O₃ in the Zn||Bi₂O₃@Ag₂O MBs compared to pure Zn||Bi₂O₃ MBs, resulting in a high total capacity that is above 2.1 times higher than the combined discharge capacities of two individual MBs. As a result, the Zn||Bi₂O₃@Ag₂O MBs deliver a high areal capacity of 16,561.5 μAh cm⁻², competitive with all reported aqueous Zn-based MBs, as well as high-performance dual-ion and Li/K/Na-ion MBs. More importantly, even at a power density of -13,550 μW cm⁻², they provide a high areal energy density of -19,000 μWh cm⁻², which can represent up to one order of magnitude higher than some recent aqueous MBs reported. Furthermore, the constructed microdevice can maintain a MSC-level or even higher power density (up to 23,231.8 μW cm⁻²). This work offers a facile and effective strategy for the development of miniaturized batteries with unprecedented areal capacity and energy density, paving the way for next-generation intelligent integrated electronic devices.

Methods

Synthesis of Bi₂O₃

Typically, 2.91 g of Bi(NO₃)₃·5H₂O (99.9%, 3AChem) and 1.28 g of Na₂SO₄ (99%, 3AChem) were dissolved in 120 mL of deionized water and stirred at room temperature for 1 h. Next, 120 mL of 0.45 M NaOH (98.0%, Aladdin) solution was added dropwise to the mixture. The resulting white dispersion was then heated in an oil bath at 60 °C for 2 h, during which the dispersion transitioned from white to light yellow. The mixture was left to stand for a brief period, allowing the formation of a yellow precipitate. The precipitate was washed with deionized water until the pH reached 7, and then dried in an oven at 80 °C overnight to obtain Bi₂O₃ powder.

The preparation of PVA-KOH gel electrolyte

Electrolytes were prepared by first formulating KOH/zinc acetate (Zn(Ac)₂) solutions at concentrations of 2 m, 6 m, and 10 m (m: mol kg_{water}⁻¹) with a fixed KOH:Zn(Ac)₂ molar ratio of 20:1. Polyvinyl alcohol (PVA, 0.44 g) was dissolved in 2 mL of deionized water at 80 °C under continuous stirring until a clear, homogeneous solution was obtained. Subsequently, 2 mL of the KOH/Zn(Ac)₂ solutions (2 m, 6 m, and 10 m) were slowly added to the PVA solution under stirring until homogeneous. The mixtures were then left to stand at room temperature for 0.5–1 h, yielding PVA/KOH/Zn(Ac)₂ hydrogel electrolytes with final concentrations of approximately 1 m, 3 m, and 5 m, respectively.

The fabrication of Zn||Bi₂O₃@Ag₂O microelectrodes and micro-batteries

First, conductive graphite paper (thickness: 0.05 mm) was precisely patterned into interdigital microelectrodes using laser direct-writing technology, based on a pre-designed pattern. The dimensions of the microelectrodes were shown in Fig. S48 (width: 0.7 mm; gap: 2.5 mm). Next, commercial Ag₂O (99.99%, Aladdin) was mixed with Bi₂O₃ in a mass ratio of 2:1 (The loading mass of Ag₂O and Bi₂O₃ is 80 mg cm⁻² and 40 mg cm⁻², respectively). The resulting composite was then blended with Super P (TIMCAL) and PVDF (Arkema Kynar) in a mass ratio of 8:1:1, using N-methyl-2-pyrrolidone (NMP, 99.0%, Aladdin) as the solvent. This mixture was coated onto the interdigital graphite paper microelectrodes to form the positive electrodes, with a total loading of approximately 120 mg cm⁻². Zinc powder (99.99%, Aladdin) was then mixed with Super P and PVDF in the same mass ratio (8:1:1), using NMP as the solvent, and coated onto the interdigital microelectrodes as the negative electrodes (The loading mass of Zn negative electrode: 50 mg cm⁻²). The positive and negative electrodes were carefully positioned onto a custom stainless-steel template attached to polyimide tape, resulting in the fabrication of the Zn||Bi₂O₃@Ag₂O microelectrodes. Finally, flexible micro-batteries were assembled by directly applying the PVA/KOH/Zn(Ac)₂ hydrogel electrolyte onto the interdigital microelectrodes.

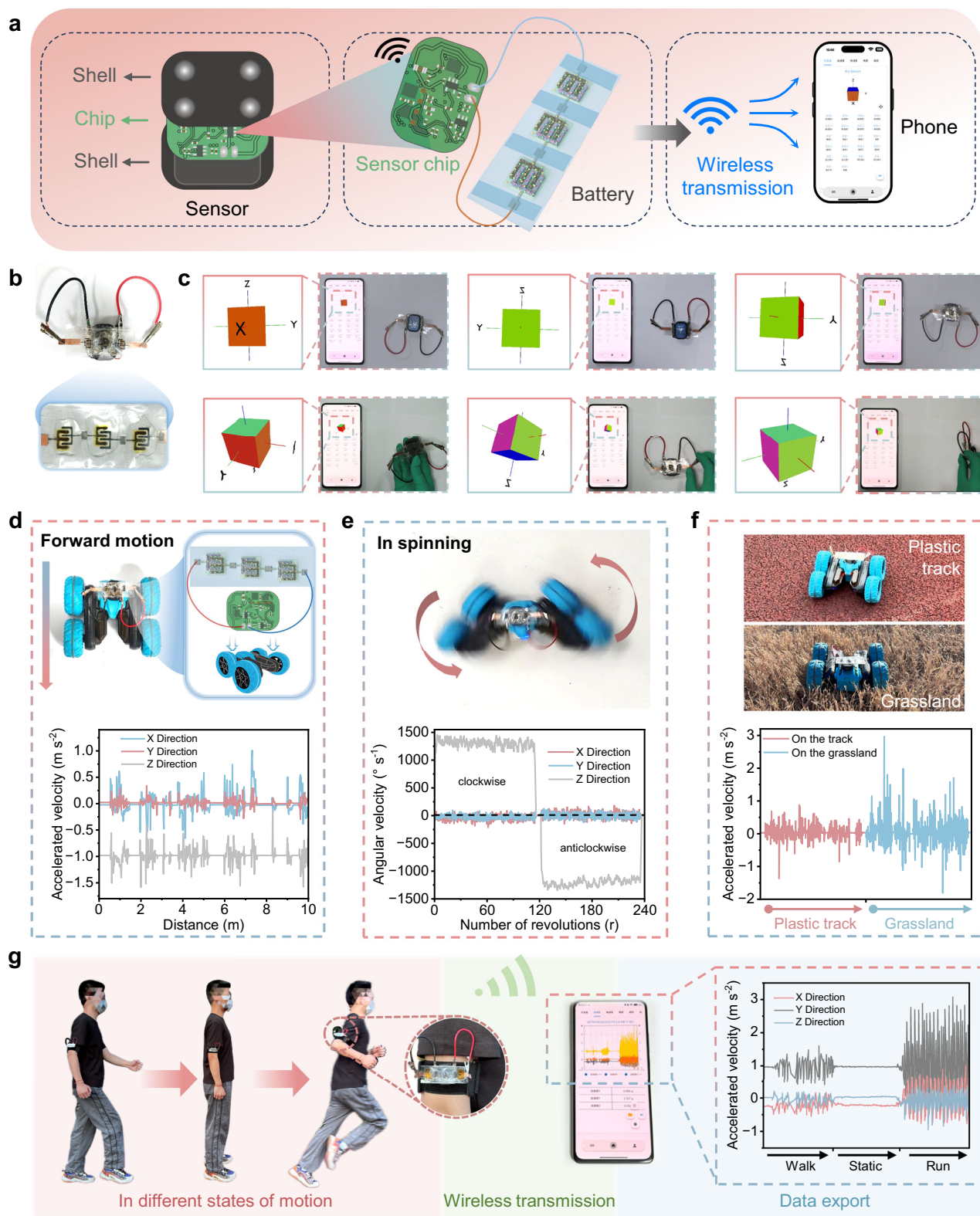


Fig. 7 | Wireless intelligent integration of Zn||Bi₂O₃@Ag₂O MBs for sensor applications. **a** Schematic of the integration of Zn||Bi₂O₃@Ag₂O MBs with sensors, enabling wireless data transmission to the mobile phone. **b** Optical photograph of the Zn||Bi₂O₃@Ag₂O MBs connected to the sensors. **c** Mobile phone wirelessly receiving signals from sensors powered by Zn||Bi₂O₃@Ag₂O MBs. The sensor

monitors the motion states of toy cars in various conditions: **d** regular movement, **e** rotational motion, and **f** across different surfaces. **g** Real-time monitoring of human motion states, such as walking, standing still, and running, using a sensor powered by Zn||Bi₂O₃@Ag₂O MBs integrated into wearable devices.

The fabrication of Zn||Ag₂O microelectrodes/micro-batteries

First, Ag₂O was blended with Super P and PVDF in a mass ratio of 8:1:1, using NMP as the solvent. This mixture was coated onto the interdigital graphite paper microelectrodes to form the positive electrodes, with a total loading of approximately 80 mg cm⁻². The positive electrode and zinc power negative electrode were positioned onto a custom stainless-steel template attached to polyimide tape, resulting in the fabrication of the Zn||Ag₂O microelectrode. Finally, Zn||Ag₂O micro-batteries were assembled by directly applying the PVA/3 m KOH/Zn(Ac)₂ gel electrolyte onto the interdigital microelectrodes.

The fabrication of Zn||Bi₂O₃ microelectrodes/micro-batteries

Zn||Bi₂O₃ microelectrode was similarly fabricated by mixing Bi₂O₃, Super P and PVDF in the mass ratio of 8:1:1, with NMP as the solvent. The mixture was coated onto the interdigital graphite paper microelectrodes to form the positive electrodes, with a total loading of approximately 40 mg cm⁻². The positive electrode and zinc power negative electrode were positioned onto a custom stainless-steel template attached to polyimide tape, resulting in the fabrication of the Zn||Bi₂O₃ microelectrode. Finally, Zn||Bi₂O₃ micro-batteries were assembled by directly applying the PVA/3 m KOH/Zn(Ac)₂ gel electrolyte onto the interdigital microelectrodes.

Characterizations

The morphologies of the samples were characterized using a scanning electron microscope (SEM, JEOL JSM-7900F; Voltage: 5.0 kV; Probe current: 76.2 μA) and a transmission electron microscope (TEM, Tecnai G20). X-ray diffraction (XRD) tests of the active materials were conducted on a Ultimal IV system with Cu Kα radiation. The test range was 20–80° and the scan rate was 8°/min. X-ray photoelectron spectroscopy (XPS) measurements were performed on a Thermo Fisher EscaLab 250Xi system (Beam energy: 1486.8 eV; Spot area: 30–500 μm). For the convenience of XRD and XPS characterization, CR2032 coin cells were assembled for battery testing. Graphite paper (thickness: 0.05 mm; diameter: 10 mm) was used as the cathode current collector, glass fiber (diameter: 16 mm, GF/D, Whatman) served as the separator, zinc foil (thickness: 0.02 mm; diameter: 10 mm, 99.99%, Canrd) was employed as the anode, and the electrolyte volume was fixed at 200 μL. Fourier-transform infrared (FT-IR) spectra were recorded using a BRUKER INVENIO spectrometer, and the wavelength range tested was between 400 and 2000 cm⁻¹ with a resolution of 4 cm⁻¹, scan rate of 60 cm⁻¹ s⁻¹. The electrical conductivity of the active material powders was measured using a TH2515 DC resistance tester. In situ XRD tests were performed using a powder X-ray diffractometer (Bruker D8 Advance, Germany) with Cu Kα radiation. The diffraction angle range was between 20 and 80°, and the cells were assembled with a beryllium window serving as the current collector.

Electrochemical measurements

All electrochemical measurement were performed using MBs. The MBs were connected to copper foil (thickness: 0.01 mm) using conductive silver glue. All tests were carried out in an open-air environment at average temperature of 28 ± 2 °C. The PVA/KOH gel electrolyte amount used in each MB was 400 μL, unless otherwise specified.

The electrochemical performance of the fabricated batteries was evaluated through galvanostatic cycling at various current densities and galvanostatic intermittent titration technique (GITT) using a LANHE CT3002A cyler. Cyclic voltammetry (CV) and electrochemical impedance spectroscopy (EIS) were conducted using a Solartron EnergyLab (Ametek) system.

For Zn||Bi₂O₃@Ag₂O MBs, CV was tested in the voltage range of 0.2–2.1 V at different scan rates. GCD profile was tested in the voltage range of 0.2–2.1 V at different current densities. EIS spectra were

recorded with a frequency ranging from 0.1 Hz to 1000 kHz (10 data points per decade of frequency). GITT curves were recorded with taking ten data points per second. For Zn||Bi₂O₃ MBs, CV was tested in the voltage range of 0.2–1.5 V at 0.6 V s⁻¹. GCD profile was tested in the voltage range of 0.2–1.5 V at different current densities. Zn||Ag₂O MBs, CV was tested in the voltage range of 1.2–2.1 V at 0.6 V s⁻¹. GCD profile was tested in the voltage range of 1.2–2.1 V at current density of 18 mA cm⁻². Gravimetric specific capacity and energy density were calculated based on the mass of the active materials, Bi₂O₃ and Ag₂O. For the Zn||Bi₂O₃@Ag₂O micro-batteries, the total area (0.18 cm²) of both the positive and negative electrode was considered in the calculations (Note: this area corresponds to the contact area between the electrolyte and electrodes, as shown in Fig. S49). Volumetrically, the microdevice has a volume of approximately 0.00855 cm³, which accounts for the combined thickness of the positive electrode, negative electrode, and the graphite paper current collector. The ionic conductivity of the gel electrolyte was determined as follows. The gel electrolyte was sandwiched between two titanium foil sheets (thickness: 0.06 mm), which served as electrodes. Titanium foil was chosen for its chemical stability in alkaline environments and good electrical conductivity. EIS was performed using a two-electrode configuration, with the titanium foils connected to the impedance analyzer. The real contact area (*A*) between the gel electrolyte and the titanium foils, as well as the electrode spacing (corresponding to the gel thickness *L*), were measured with calipers to minimize error. The ionic conductivity (*σ*) of the gel electrolyte was calculated according to the equation^{4,32}:

$$\sigma = \frac{L}{RA} \quad (4)$$

where *L* is the gel thickness, *R* is the ohmic resistance obtained from the *x*-axis intercept of the Nyquist plot in EIS measurements, and *A* is the real contact area between the gel electrolyte and the titanium foils. The authors affirm that human research participants provided informed consent for publication of the images in Fig. 7g.

Data availability

All data that support the findings of this study are presented in the manuscript and Supplementary Information or are available from the corresponding author upon request. Source data are provided with this paper.

References

- Kyeremateng, N. A., Brousse, T. & Pech, D. Microsupercapacitors as miniaturized energy-storage components for on-chip electronics. *Nat. Nanotechnol.* **12**, 7–15 (2017).
- Huang, P. et al. On-chip and freestanding elastic carbon films for micro-supercapacitors. *Science* **351**, 691–695 (2016).
- Kwon, Y. W. et al. Power-integrated, wireless neural recording systems on the cranium using a direct printing method for deep-brain analysis. *Sci. Adv.* **10**, eadn3784 (2024).
- Jin, X. et al. A flexible aqueous zinc-iodine microbattery with unprecedented energy density. *Adv. Mater.* **34**, 2109450 (2022).
- Niu, K. et al. A self-healing aqueous ammonium-ion micro batteries based on PVA-NH₄Cl hydrogel electrolyte and MXene-integrated perylene anode. *Nano Research Energy* **3**, e9120127 (2024).
- Yuan, Y. et al. Laser maskless fast patterning for multitype micro-supercapacitors. *Nat. Commun.* **14**, 3967 (2023).
- Lei, Z. et al. Nanoelectrode design from microminiaturized honeycomb monolith with ultrathin and stiff nanoscaffold for high-energy micro-supercapacitors. *Nat. Commun.* **11**, 299 (2020).

8. Wang, S., Ma, J., Shi, X., Zhu, Y. & Wu, Z.-S. Recent status and future perspectives of ultracompact and customizable micro-supercapacitors. *Nano Res. Energy* **1**, e9120018 (2022).
9. Wang, Y. et al. Fixture-free omnidirectional prestretching fabrication and integration of crumpled in-plane micro-supercapacitors. *Sci. Adv.* **8**, eabn8338 (2022).
10. Wang, S. et al. Monolithically integrated micro-supercapacitors with high areal number density produced by surface adhesive-directed electrolyte assembly. *Nat. Commun.* **15**, 2850 (2024).
11. Sun, P., Li, X., Shao, J. & Braun, P. V. High-performance packaged 3D lithium-ion microbatteries fabricated using imprint lithography. *Adv. Mater.* **33**, 2006229 (2021).
12. Zheng, S. et al. Multitasking MXene inks enable high-performance printable microelectrochemical energy storage devices for all-flexible self-powered integrated systems. *Adv. Mater.* **33**, 2005449 (2021).
13. Pikul, J. H., Zhang, H. G., Cho, J., Braun, P. V. & King, W. P. High-power lithium ion microbatteries from interdigitated three-dimensional bicontinuous nanoporous electrodes. *Nat. Commun.* **4**, 1732 (2013).
14. Ning, H. et al. Holographic patterning of high-performance on-chip 3D lithium-ion microbatteries. *Proc. Natl. Acad. Sci. USA.* **112**, 6573–6578 (2015).
15. Liu, Q. et al. The first flexible dual-ion microbattery demonstrates superior capacity and ultrahigh energy density: small and powerful. *Adv. Funct. Mater.* **30**, 2002086 (2020).
16. Zheng, S. et al. Ionogel-based sodium ion micro-batteries with a 3D Na-ion diffusion mechanism enable ultrahigh rate capability. *Energy Environ. Sci.* **13**, 821–829 (2020).
17. Ma, J. et al. 3D printing flexible sodium-ion microbatteries with ultrahigh areal capacity and robust rate capability. *Adv. Mater.* **34**, 2205569 (2022).
18. Song, L. et al. Recent progress and challenges in interdigital microbatteries: Fabrication, functionalization and integration. *J. Energy Chem.* **78**, 294–314 (2023).
19. Naresh, N. et al. Advanced 3D micro-electrodes for on-chip zinc-ion micro-batteries. *Adv. Funct. Mater.* **35**, 2413777 (2024).
20. Qu, Z. et al. A photolithographable electrolyte for deeply rechargeable Zn microbatteries in on-chip devices. *Adv. Mater.* **36**, 2310667 (2024).
21. Zhu, M. et al. A patternable and in situ formed polymeric zinc blanket for a reversible zinc anode in a skin-mountable micro-battery. *Adv. Mater.* **33**, 2007497 (2021).
22. Yang, W. et al. 3D macroporous frame-based microbattery with ultrahigh capacity, energy density, and integrability. *Adv. Energy Mater.* **13**, 2300574 (2023).
23. Li, X. et al. All-direct laser patterning zinc-based microbatteries. *Adv. Funct. Mater.* **34**, 2314060 (2024).
24. Li, P. et al. Dynamically resettable electrode-electrolyte interface through supramolecular sol-gel transition electrolyte for flexible zinc batteries. *Angew. Chem. Int. Ed.* **62**, e202300705 (2023).
25. Shi, J. et al. An ultrahigh energy density quasi-solid-state zinc ion microbattery with excellent flexibility and thermostability. *Adv. Energy Mater.* **9**, 1901957 (2019).
26. Wang, X. et al. 2D amorphous V_2O_5 /graphene heterostructures for high-safety aqueous Zn-ion batteries with unprecedented capacity and ultrahigh rate capability. *Adv. Energy Mater.* **10**, 2000081 (2020).
27. Yang, W. et al. Rechargeable zinc-ammonium hybrid microbattery with ultrahigh energy and power density. *Matter* **6**, 3006–3020 (2023).
28. Zhao, J. et al. A smart flexible zinc battery with cooling recovery ability. *Angew. Chem. Int. Ed.* **56**, 7871–7875 (2017).
29. Tian, Z. et al. Ultrafast rechargeable Zn micro-batteries endowing a wearable solar charging system with high overall efficiency. *Energy Environ. Sci.* **14**, 1602–1611 (2021).
30. Hao, Z. et al. On-chip Ni-Zn microbattery based on hierarchical ordered porous $Ni@Ni(OH)_2$ microelectrode with ultrafast ion and electron transport kinetics. *Adv. Funct. Mater.* **29**, 1808470 (2019).
31. Lu, Y. et al. 3D printed flexible zinc ion micro-batteries with high areal capacity toward practical application. *Adv. Funct. Mater.* **34**, 2310966 (2024).
32. Dai, C. et al. Fast constructing polarity-switchable zinc-bromine microbatteries with high areal energy density. *Sci. Adv.* **8**, eabo6688 (2022).
33. Li, Y. et al. Plasmonic hot electrons from oxygen vacancies for infrared light-driven catalytic CO_2 reduction on Bi_2O_{3-x} . *Angew. Chem. Int. Ed.* **60**, 910–916 (2021).
34. Shin, J. et al. Deposition of ZnO on bismuth species towards a rechargeable Zn-based aqueous battery. *Phys. Chem. Chem. Phys.* **18**, 26376–26382 (2016).
35. Santos, F. et al. In situ synchrotron x-ray diffraction study of Zn|| Bi_2O_3 electrodes prior to and during discharge of Zn-air batteries: Influence on ZnO deposition. *Electrochim. Acta* **281**, 133–141 (2018).
36. Lee, S. et al. Improvement in self-discharge of Zn anode by applying surface modification for Zn-air batteries with high energy density. *J. Power Sources* **227**, 177–184 (2013).
37. Zeng, Y. et al. Flexible ultrafast aqueous rechargeable Ni//Bi battery based on highly durable single-crystalline bismuth nanostructured anode. *Adv. Mater.* **28**, 9188–9195 (2016).
38. Ba, D. et al. Directly grown nanostructured electrodes for high-power and high-stability alkaline nickel/bismuth batteries. *Sci. China Mater.* **62**, 487–496 (2019).
39. Zeng, Y. et al. Engineering high reversibility and fast kinetics of Bi nanoflakes by surface modulation for ultrastable nickel-bismuth batteries. *Chem. Sci.* **10**, 3602–3607 (2019).
40. Xiong, T. et al. Bismuth ion battery-A new member in trivalent battery technology. *Energy Storage Mater.* **25**, 100–104 (2020).
41. Gujar, T. et al. Electrosynthesis of Bi_2O_3 thin films and their use in electrochemical supercapacitors. *J. Power Sources* **161**, 1479–1485 (2006).
42. Zhou, D. et al. An innovative $Bi_{12}SiO_{20}$ multistage cubic nanospheres cathode for high-performance Bi//Zn battery. *Chem. Eur. J.* **29**, e202203500 (2023).
43. Lorca, S. et al. Characterization of a new rechargeable Zn/PVA-KOH/ Bi_2O_3 battery: structural changes of the Bi_2O_3 electrode. *Sustain. Energy Fuels* **4**, 4497–4505 (2020).
44. Luo, X. et al. Regulating the intermediate process of zinc-bismuth batteries by iodide ions. *ACS Energy Lett.* **8**, 3569 (2023).
45. Ma, W., Li, J., Wang, H., Lei, C. & Liang, X. High efficiency alkaline iodine batteries with multi-electron transfer enabled by Bi/ Bi_2O_3 redox mediator. *Angew. Chem. Int. Ed.* **63**, e202410994 (2024).
46. Wang, D. et al. A zinc battery with ultra-flat discharge plateau through phase transition mechanism. *Nano Energy* **71**, 104583 (2020).
47. Kumar, R. et al. All-printed, stretchable Zn- Ag_2O rechargeable battery via, hyperelastic binder for self-powering wearable electronics. *Adv. Energy Mater.* **7**, 1602096 (2017).
48. Kumar, R. et al. Scaling printable Zn- Ag_2O batteries for integrated electronics. *Adv. Energy Mater.* **9**, 1803645 (2019).
49. Zamarayeva, A. M. et al. Flexible and stretchable power sources for wearable electronics. *Sci. Adv.* **7**, e1602051 (2017).
50. Yin, L. et al. High performance printed AgO -Zn rechargeable battery for flexible electronics. *Joule* **5**, 228 (2021).

51. Li, C. et al. High-performance quasi-solid-state flexible aqueous rechargeable Ag-Zn battery based on metal-organic framework-derived Ag nanowires. *ACS Energy Lett.* **3**, 2761 (2018).
52. Xie, W. et al. Advancements in achieving high reversibility of zinc anode for alkaline zinc-based batteries. *Adv. Mater.* **36**, 2306154 (2024).
53. Zhu, M. et al. Light-permeable, photoluminescent microbatteries embedded in the color filter of a screen. *Energy Environ. Sci.* **11**, 2414–2422 (2018).
54. Wang, X. et al. Scalable fabrication of printed Zn//MnO₂ planar micro-batteries with high volumetric energy density and exceptional safety. *Natl. Sci. Rev.* **7**, 64–72 (2020).
55. Zhang, X. et al. Fully printed and sweat-activated micro-batteries with lattice-match Zn/MoS₂ anode for long-duration wearables. *Adv. Mater.* **34**, 2412844 (2024).
56. Jin, X. et al. Solvent polarity-induced regulation of cation solvation sheaths for high-voltage zinc-based batteries with a 1.94 V discharge platform. *Angew. Chem. Int. Ed.* **64**, e202418682 (2024).
57. Zhao, B. et al. A flexible, heat-resistant and self-healable “rocking-chair” zinc ion microbattery based on MXene-TiS₂ (de)intercalation anode. *J. Power Sources* **504**, 230076 (2021).
58. Wang, Y. et al. Wearable textile-based Co-Zn alkaline microbattery with high energy density and excellent reliability. *Small* **16**, 2000293 (2020).
59. Lee, S. H. et al. Zinc-ion microbatteries with high operando dynamic stretchability designed to operate in extreme environments. *Adv. Funct. Mater.* **34**, 2310571 (2024).
60. Li, Y.-Q. et al. Dual-phase nanostructuring of layered metal oxides for high-performance aqueous rechargeable potassium ion micro-batteries. *Nat. Commun.* **10**, 4292 (2019).
61. Wang, X. et al. High-voltage aqueous planar symmetric sodium ion micro-batteries with superior performance at low-temperature of -40°C. *Nano Energy* **82**, 105688 (2021).
62. Zhang, Y. et al. Multi-layer printable lithium ion micro-batteries with remarkable areal energy density and flexibility for wearable smart electronics. *Small* **18**, 2104506 (2022).
63. Liu, B. et al. Electrochemically exfoliated chlorine-doped graphene for flexible all-solid-state micro-supercapacitors with high volumetric energy density. *Adv. Mater.* **34**, 2106309 (2022).
64. Zhang, Y. et al. Flexible self-powered integrated sensing system with 3D periodic ordered black phosphorus@MXene thin-films. *Adv. Mater.* **33**, 2007890 (2021).
65. Li, K. et al. 4D printing of MXene hydrogels for high-efficiency pseudocapacitive energy storage. *Nat. Commun.* **13**, 6884 (2022).
66. Shao, Y. et al. Room-temperature high-precision printing of flexible wireless electronics based on MXene inks. *Nat. Commun.* **13**, 3223 (2022).
67. Zhang, C. J. et al. High-performance MXene-based materials for energy storage and sensing applications. *Nat. Commun.* **10**, 1795 (2019).
68. Jin, X. et al. An aqueous anti-freezing and heat-tolerant symmetric microsupercapacitor with 2.3 V output voltage. *Adv. Energy Mater.* **11**, 2101523 (2021).
69. Choi, C. et al. Photopatternable hydroxide ion electrolyte for solid-state micro-supercapacitors. *Joule* **5**, 2466–2478 (2021).
70. Song, L. et al. Pure aqueous planar microsupercapacitors with ultrahigh energy density under wide temperature ranges. *Adv. Funct. Mater.* **32**, 2203270 (2022).
71. Zhang, W. et al. Kinetics-boosted effect enabled by zwitterionic hydrogel electrolyte for highly reversible zinc anode in zinc-ion hybrid micro-supercapacitors. *Adv. Energy Mater.* **12**, 2202219 (2022).
72. Zhang, P. et al. High-performance micro-supercapacitors with flexible carbon nanostructure electrodes. *Adv. Mater.* **31**, 1806005 (2019).
73. Sun, G. et al. A capacity recoverable zinc-ion micro-supercapacitor. *Energy Environ. Sci.* **11**, 3367–3374 (2018).
74. Fan, Y. et al. Planar Zn-ion microcapacitors with high-capacity activated carbon anode and VO₂ (B) cathode. *Nano Lett.* **24**, 10874–10882 (2024).
75. Cao, Z., Liang, G., Ho, D., Zhi, C. & Hu, H. Interlayer injection of low-valence Zn atoms to activate MXene-based micro-redox capacitors with battery-type voltage plateaus. *Adv. Funct. Mater.* **33**, 2303060 (2023).
76. Zhang, J. et al. Wood-like low-tortuosity thick electrode for micro-redoxcapacitor with ultrahigh areal energy density and steady power output. *Adv. Funct. Mater.* **34**, 2310775 (2023).
77. Zheng, S. et al. All-solid-state flexible planar lithium ion micro-capacitors. *Energy Environ. Sci.* **11**, 2001–2009 (2018).
78. Zheng, S. et al. All-solid-state planar sodium-ion microcapacitors with multidirectional fast ion diffusion pathways. *Adv. Sci.* **6**, 1902147 (2019).
79. El-Kady, M. F. & Kaner, R. B. Scalable fabrication of high-power graphene micro-supercapacitors for flexible and on-chip energy storage. *Nat. Commun.* **4**, 1475 (2013).
80. Yu, D. et al. Scalable synthesis of hierarchically structured carbon nanotube-graphene fibers for capacitive energy storage. *Nat. Nanotechnol.* **9**, 555–562 (2014).
81. Yang, H. et al. A metal-organic framework as a multifunctional ionic sieve membrane for long-life aqueous zinc-iodide batteries. *Adv. Mater.* **32**, 2004240 (2020).
82. Ma, L. et al. Electrocatalytic iodine reduction reaction enabled by aqueous zinc-iodine battery with improved power and energy densities. *Angew. Chem. Int. Ed.* **60**, 3791 (2021).
83. Kang, L. et al. Hierarchical spatial confinement unlocking the storage limit of MoS₂ for flexible high-energy supercapacitors. *ACS Nano* **18**, 2149 (2024).
84. Liu, S. et al. Unlocking the potential of oxygen-deficient copper-doped Co₃O₄ nanocrystals confined in carbon as an advanced electrode for flexible solid-state supercapacitors. *ACS Energy Lett.* **6**, 3011 (2021).
85. Zheng, S. et al. All-solid-state planar integrated lithium-ion micro-batteries with extraordinary flexibility and high-temperature performance. *Nano Energy* **51**, 613–620 (2018).
86. Cao, D. et al. 3D printed high-performance lithium metal micro-batteries enabled by nanocellulose. *Adv. Mater.* **31**, 1807313 (2019).
87. Shi, J. et al. High-performance MoO_{3-x}/MXene cathodes for zinc-ion batteries based on oxygen vacancies and electrolyte engineering. *Nano Energy* **91**, 106651 (2022).
88. Wang, S. et al. Flexible electronic systems via electrohydrodynamic jet printing: A MnSe@rGO cathode for aqueous zinc-ion batteries. *ACS Nano* **17**, 13256–13268 (2023).

Acknowledgements

The authors acknowledge the financial support from the National Natural Science Foundation of China (NSFC) (No. 22479130), the Natural Science Foundation of Henan (No. 252300421170), NSFC (No. 22509191), the National Science Foundation of Henan (No. 252300423744).

Author contributions

X. Jin, X. Xiu, and L. Song designed the project. X. Xiu performed most of the experiments and characterization. X. Xiu, X. Jin, L. Song, M. Li, X. Li, and Z. Quan contributed to the structural characterizations,

electrochemical measurements, and manuscript revisions. X. Jin, X. Xiu, L. Song, L. Qu, and Z. Zhou wrote and modified the paper. All the authors discussed the data and the manuscript.

Competing interests

The authors declare no competing interests.

Additional information

Supplementary information The online version contains supplementary material available at

<https://doi.org/10.1038/s41467-026-69317-z>.

Correspondence and requests for materials should be addressed to Xuting Jin, Liangti Qu or Zhen Zhou.

Peer review information *Nature Communications* thanks Kai Yang, Buddha Deka Boruah and the other anonymous reviewer(s) for their contribution to the peer review of this work. A peer review file is available.

Reprints and permissions information is available at <http://www.nature.com/reprints>

Publisher's note Springer Nature remains neutral with regard to jurisdictional claims in published maps and institutional affiliations.

Open Access This article is licensed under a Creative Commons Attribution-NonCommercial-NoDerivatives 4.0 International License, which permits any non-commercial use, sharing, distribution and reproduction in any medium or format, as long as you give appropriate credit to the original author(s) and the source, provide a link to the Creative Commons licence, and indicate if you modified the licensed material. You do not have permission under this licence to share adapted material derived from this article or parts of it. The images or other third party material in this article are included in the article's Creative Commons licence, unless indicated otherwise in a credit line to the material. If material is not included in the article's Creative Commons licence and your intended use is not permitted by statutory regulation or exceeds the permitted use, you will need to obtain permission directly from the copyright holder. To view a copy of this licence, visit <http://creativecommons.org/licenses/by-nc-nd/4.0/>.

© The Author(s) 2026